# Graphene Quantum Dots Coated $VO_2$ Arrays for Highly Durable Electrodes for Li and Na Ion Batteries

Dongliang Chao,[†,&] Changrong Zhu,[†,&] Xinhui Xia,[†] Jilei Liu,[†] Xiao Zhang,[§] Jin Wang,[§] Pei Liang,[#] Jianyi Lin,[§] Hua Zhang,[‡] Ze Xiang Shen,*[,†,‡] and Hong Jin Fan*[,†]

[†] *School of Physical and Mathematical Sciences, Nanyang Technological University, Singapore 637371, Singapore*

[‡] *School of Materials Science and Engineering, Nanyang Technological University, Singapore 639798, Singapore*

[§] *Energy Research Institute @ NTU, Nanyang Technological University, Singapore 639798, Singapore*

[#] *College of Optical and Electronic Technology, China Jiliang University, Hangzhou 310038, China*

## Abstract

Nanoscale surface engineering is playing important role in enhancing the performance of battery electrode. $VO_2$ is one of high-capacity but less-stable materials, and has been used mostly in the form of powders for Li-ion battery cathode with mediocre performance. In this work, we design a new type of binder-free cathode by bottom-up growth of bi-face $VO_2$ arrays directly on a graphene network for both high-performance Li-ion and Na-ion battery cathodes. More importantly, graphene quantum dots (GQDs) are coated onto the $VO_2$ surfaces as a highly efficient surface "sensitizer" and protection to further boost the electrochemical properties. The integrated electrodes deliver a Na storage capacity of 306 mAh/g at 100 mA/g, and a capacity of more than 110 mAh/g after 1500 cycles at 18 A/g. Our result on Na-ion battery may pave the way to next-generation postlithium batteries.

*Keywords: vanadium oxides; sodium ion battery; lithium ion battery; graphene quantum dots; nanoarray electrodes*

Due to the exhaust of traditional non-renewable fossil resources and serious environment pollution, there has been an increasing demand in sustainable and clean energy sources. Both energy harvesting from nature, and storage via battery and supercapacitor technologies are the center of current research worldwide.[1-4] Li ion batteries (LIBs) have been a favorable power source device in electronics and electric vehicles because of their advantages of high capacity, long cycle life and environmental benignity.[5-7] While the present LIBs technology is quite mature, ambient temperature Na ion batteries (NIBs) are receiving increasing attentions partly because of the wide availability of Na and thus potentially low cost.[8] There are recent reports available on a number of new materials such as layered transition metal oxides P2-$Na_xCoO_2$,[9] $Na_x[Fe_{1/2}Mn_{1/2}]O_2$,[10] cubic $Na_xMnFe(CN)_6$,[11] NASICON-type $Na_3V_2(PO_4)_3$,[12] and fluoride-based $ReO_3$-type $FeF_3$.[13] These pioneering work in NIBs opened a new window, albeit the fact that the reported capacities are still very low (less than 200 mAh/g) compared to LIBs.

Vanadium oxide has been long regarded as a promising electrode material for LIBs owing to its high capacity, low cost and abundant sources.[4, 14-16] In particular, vanadium dioxide stands out because of its unique $VO_2$ (B) bilayers formed from edge-sharing $VO_6$ octahedra, rapid lithium ion diffusion rate and higher capacity than other types vanadium oxides.[15, 17] So far, various forms of $VO_2$ nanostructures for LIBs cathode materials have been prepared, such as $VO_2$ nanoparticles,[18] $VO_2$ nanowires,[19] $VO_2$ nanobelts,[20] star-like $VO_2$ mesocrystals,[21] and $VO_2$ nanowires assembled hollow microspheres[17] (see a complete list in Table S1 in the Supporting Information). While $VO_2$-related nanomaterials are being extensively studied for LIBs, their application in NIB has not been explored. It is noted that $V_2O_5$ nanoparticles[3] and $V_2O_5$ nanobelts[22] with larger lattice spacing have been recently synthesized and demonstrated good sodium ion storage performance. Despite these efforts, the major problem is that, these materials suffer from fast capacity fading and poor high-rate performance, probably due to reasons such as self-aggregation, dissolution and the fast increased charge transfer resistance during cycles. Therefore, tailored nanoarchitecture design and additional surface engineering of active materials are desirable, which can both secure high surface conductivity and sustain the structure integrity for long-time and high-rate cycling.

In this letter, we demonstrate our nanostructure tailored $VO_2$ array as the cathode for both LIBs and NIBs with significantly improved electrochemical properties (high-rate capacity tolerance and long-term stability). Our nanostructured electrode design offers the following

advantages.

(a) *Binder-free electrode rendered by bi-face graphene foam*. In our design, the graphene foam (GF, also known as ultrathin graphite foam) acts as both scaffold for the bottom-up growth of $VO_2$ and an efficient current collector. Compared to other common electrode substrates (e.g., Ni foam, carbon cloth, metal foils), GF are super light, more porous, and still highly conductive. Most importantly, the use of GF eliminates the necessity of binder (PTFE, PVDF, etc.), conductive additive (carbon black, etc.) and current collectors (Al/Cu foil), so that it further decreases the weight of the full cell. In the particular case of NIB, most of current electrode materials for NIBs are in powder form and requires conductive additives and binders. However, some conductive additives contributes to capacity during sodiation (50 –150 mAh/g).[23, 24] It is also found that the widely used binder PVDF accelerates the deterioration of electrode during sodiation.[25, 26] Therefore, a free-standing and binder-free electrode would be essential for NIBs.

(b) *$VO_2$ nanobelts beneficial to fast ion diffusion*. As the diffusion time of ions (t) is proportional to the square of the diffusion length (L): $t \approx L^2/D$,[15] another effective strategy to enhance the rate performance is to reduce the dimensions and thickness of the active material. In our electrode design, the $VO_2$ nanobelt nanoarray effectively reduces the $Li^+$ and $Na^+$ diffusion length, and also enhances the electrolyte mobility. This is important in boosting the high-rate performance in both Li and Na ions storage.

(c) *Graphene quantum dots as an effective sensitizer and stabilizer*. Graphene quantum dots (GQDs, small graphene flakes usually smaller than 100 nm in size and less than 10 layers in thickness) have interesting optical properties due to tunable size and surface chemistry.[27] As an emerging attractive carbon material, GQDs have shown their value-added function in LEDs,[28] supercapacitors,[29] solar cells,[30, 31] oxygen reduction reaction,[32] and sensors.[33] To the best of our knowledge, application of GQDs in batteries has not been reported. Herein, functionalized GQDs were coated onto individual $VO_2$ nanobelt by electrophoresis deposition. The homogeneous GQDs covering can effectively separate the $VO_2$ nanobelts from each other and thus avoid agglomeration, and also minimize the dissolution of active materials, especially during the long-term cycling. Moreover, the “stacking” feature of the GQDs layer can provide extra $Na^+$ storage venues between the graphene flakes (viz., nanocavities).[34] It is noted that $VO_2$ composites with graphene have been reported for LIB application ($VO_2$/graphene ribbons[15] and $VO_2$ nanotube/graphene[35]), but a homogeneous coating is still challenging. The electrophoresis

deposition applied in this study is a facile technique for controllable and uniform coating of GQDs onto various metal oxide nanostructures.

With the above merits, our 3D GF-supported, GQDs-coated $VO_2$ nanobelt arrays electrodes exhibit superior high-rate capability and cycling stability both in LIBs and NIBs.

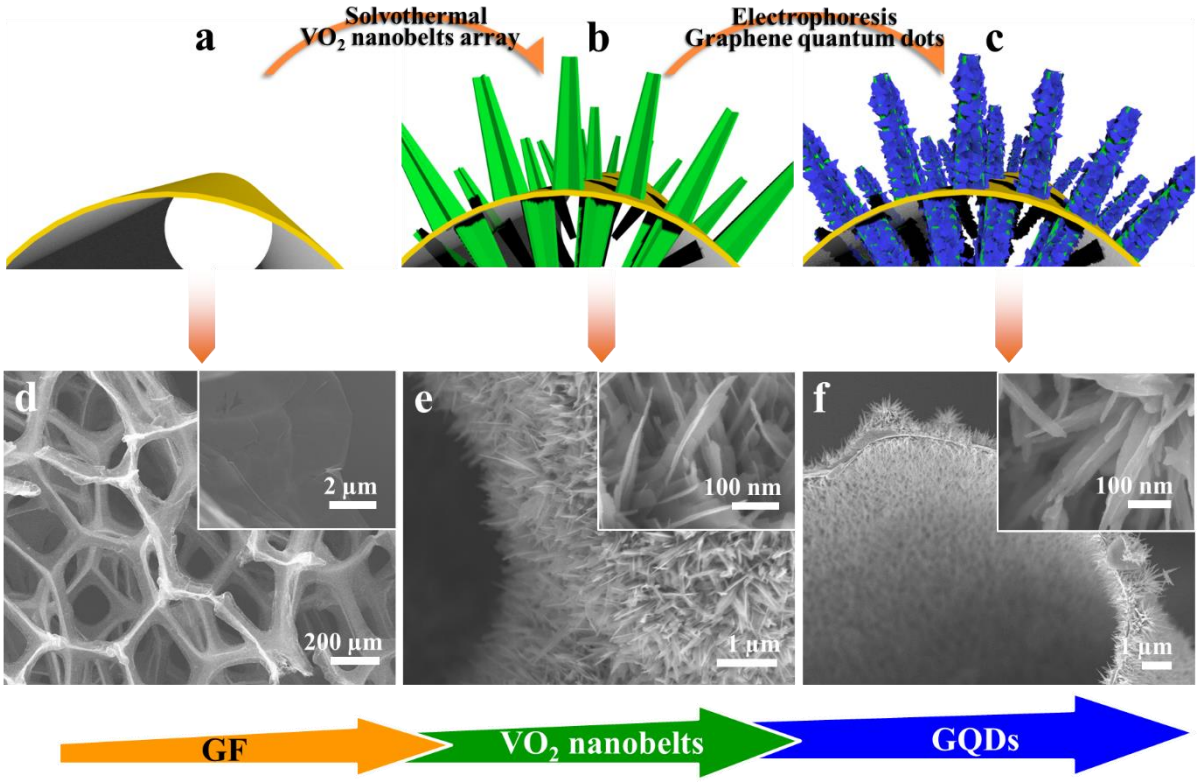


**Figure 1.** Fabrication processes of GF supported GQDs-coated $VO_2$ nanobelts array. (a-c) Schematics of the fabrication process. The yellow basis represent the GF substrate. The green arrays represent $VO_2$ nanoarrays, and the blue covering represents the GQDs; (d-f) The corresponding SEM images (fine structure in inset).

**Electrode Fabrication and Morphology.**

The synthesis procedure of the GF supported GQD-anchored $VO_2$ arrays electrode (the whole electrode structure is denoted as GVG) is illustrated in Figure 1a-c. First, CVD-grown graphene foam (Figure 1a,d) was employed as the substrate to grow $VO_2$ nanoarrays via a solvothermal process (Figure 1b, this structure is denoted as GV). As can be seen from Figure 1e, the $VO_2$ nanoarrays exhibit a homogeneous size and shape distribution. The building block

contains two intersected nanobelts (ca. 80 nm in width and ca. 15 nm in thickness). A similar structure (six-armed microspindle particle) was also observed by Mai[17] and Cao[21]. The simplified solvothermal reactions are proposed as follows:

$$V_2O_5 + 3H_2C_2O_4 \leftrightarrow 2VOC_2O_4 + 3H_2O + 2CO_2 \quad (1)$$

$$2VOC_2O_4 \leftrightarrow 2VO_2 + 3CO_2 + C \quad (2)$$

The growth mechanism is proposed to involve the "self-assembly" and "oriented crystallization" processes. During the solvothermal reaction, the $VOC_2O_4$ nucleates onto the surface of GF, where bonding between the particles reduces the overall energy. Then a belt structure formed according to the strong crystal anisotropy of monoclinic $VO_2$. Finally, two single belts coalesce together to form the intersected nanobelts architecture through the oriented attachment mechanism.[21, 36] There may be some degree of subsequent coarsening with the increase of the solvothermal time, as shown in Figure S1 (longer solvothermal time corresponds to thicker and bigger nanobelts). Detailed crystallographic details of the synthesized nanobelts will be discussed in the next part.

The interspaces between neighboring nanoarrays allow homogeneous coating of GQDs in the subsequent electrophoresis process (as well as electrolyte penetration during electrochemical tests). GQDs are negatively charged because of the carboxyl groups on the surfaces. They can be tightly immobilized onto the positively charged surface of $VO_2$ nanoarrays driven by positive bias in the electrophoresis deposition process (Figure 1c). The resulting core/shell material preserves the nanobelt array structure, except for a wrinkled surface (Figure 1f). With increasing the electrophoresis time, GQDs tend to fill up all corners of the intersected nanobelts (Figure S1f). It is thus implied that the GQDs form a "stacking card" structure during the coating. Nonetheless, in order to assure a high electrochemical kinetics, we choose an overall thickness of the GQDs layer to be around 2 nm. One can clearly see that the $VO_2$@GQD hierarchical structure grow on both the outer and inner sides of the GF skeleton, i.e., bi-face array. The bi-face array can largely increase the utilization of the skeleton and the active sites with electrolyte. Finally, the electrodes are light and bendable (see optical images in Figure S2d,f).

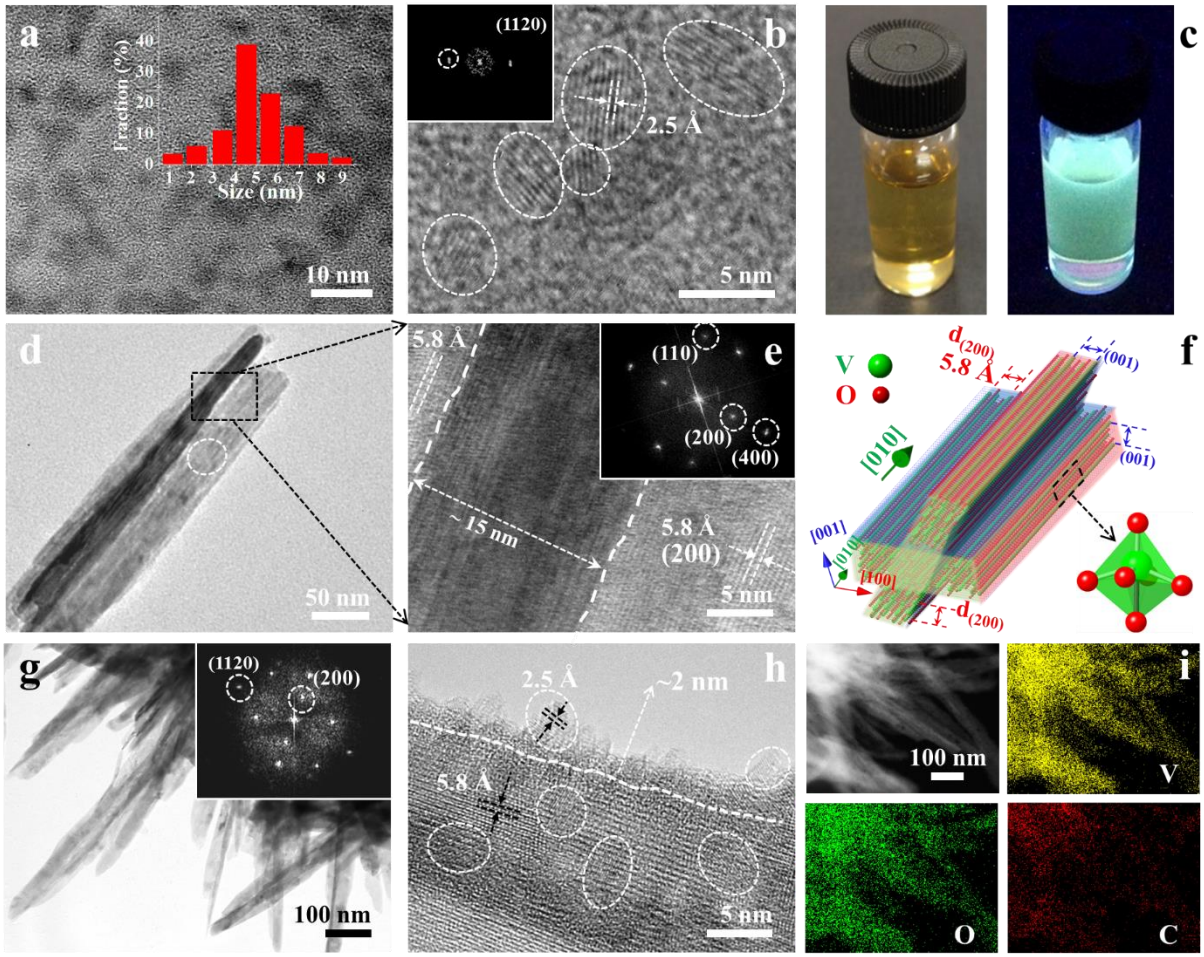


**Figure 2.** TEM characterizations. (a) TEM of GQDs with size distribution in inset; (b) HRTEM of GQDs with FFT pattern in inset; (c) Photographs of the GQD aqueous solution taken under visible light (left) and 365 nm UV light (right); (d,e) TEM and HRTEM of $VO_2$ nanoarray. Inset: FFT pattern in the [002] zone axis; (f) Geometrical model of the bilayered $VO_2$ nanobelt. The crystal planes are false colored as (100)-red, (010)-green, and (001)-blue; (g,h) TEM and HRTEM of $VO_2$@GQD nanoarray with FFT pattern in inset; (i) Dark field TEM image of $VO_2$@GQD nanoarray and the corresponding EDS mapping of V, O and C elements.

**Structure Characterization and Growth Mechanism.**

The X-ray diffraction (XRD) results in Figure S3a demonstrate the highly crystalline structure of GF (JCPDS 75-1621) and monoclinic $VO_2$ (B) (lattice parameters a = 12.07 Å, b = 3.69 Å, c = 6.43 Å, β = 106.6 °, C2/m space group, JCPDS 31-1438). After GQD coating, the

diffraction peaks of GF and $VO_2$ (B) can also be well indexed, indicating that the EPD process has negligible influence on the intrinsic crystallinity of the $VO_2$ (B). Figure S3b show the Raman spectra of GF, GV arrays and GVG nanoarrays. The characteristic peak of graphene G band at ca. 1575 $cm^{-1}$ is identified. The defect-related D band is not observed, implying the overall high quality of the GF by the CVD method. In addition to the peaks of the GF, the rest Raman peaks can be well indexed to crystalline $VO_2$.[15, 37] For GQDs, no extra XRD diffraction peaks or Raman characteristic peaks are observed because of peak overlapping with GF. To avoid this overlapping issue, $VO_2$ arrays and GQDs were also fabricated on fluorine-tin-oxide (FTO) substrates with the same method. For FTO-GQD sample, D (ca. 1350 $cm^{-1}$) and G (ca. 1580$cm^{-1}$) bands are clearly observed due to the existence of defects and functional groups of GQDs. Compared with GV arrays, these two characteristic peaks are also found after for the GVG sample, illustrating the successful fabrication of GQDs on $VO_2$ arrays.

The detailed crystal structures of the functional GQDs, bilayered $VO_2$, and GVG nanoarrays were characterized by TEM (Figure 2). A typical TEM image (Figure 2a) shows that the as-made GQDs are well-dispersed and have a typical lateral size ca. 5 nm (bandgap less than 0.5 eV according to density functional theory calculation[38, 39]). The hexagonal (1120) plane lattice spacing of 2.5 Å can be well resolved in HRTEM image (Figure 2b).[33] The light-brown GQDs solution is very stable without any noticeable precipitation after several weeks at room temperature. The solution under illumination by a 365 nm lamp emits an intense blue-green fluorescence (Figure 2c), which could be attributed to the effect of size and surface functional groups.[33, 40]

The $VO_2$ bi-layer nanobelt has two branches parallel intersected with a thickness ca. 15 nm for individual belt (Figure 2d). HRTEM from one nanobelt branch (Figure 2e) reveal clearly the lattice fringes with spacing of 5.8 Å, corresponding to the (200) lattice planes (JCPDS 31-1438). The single crystalline nature of individual nanobelt is also confirmed by FFT pattern. By considering the growth direction and lattice spacings from the HRTEM investigation, we construct the geometric model of the bilayered $VO_2$ nanobelt (Figure 2f and Figure S5). The preferred growth direction is determined by the relative high stacking rate of the "steplike" $VO_6$ octahedra along the [010] direction (the shortest bond).[41] These findings corroborate the "oriented attachment" of the single crystalline bilayered $VO_2$ nanobelts and the [010] growth direction is in agreement with literature results.[21, 41] As for the interface of $VO_2$, the longest V-O

bond is along the [001] direction (Figure S5), corresponding to the slowest growth along this direction. As a result, the (001) facets are the thinnest and predominant ones of the $VO_2$ nanobelts (Figure 2e and f). On these facets the large interlayers between the (200) crystal planes provide a facile channel for both Li and Na ion diffusion.

After the electrophoresis deposition of GQDs, the $VO_2$ nanoarrays are closely coated by a uniform GQDs layer (ca. 2 nm in thickness) with a preserved nanoarrays structure but more jagged. The HRTEM and FFT results (Figure 2h and its enlarged Figure S4) reveal the lattice fringes of both GQDs and$VO_2$, same as described above. Energy dispersive X-ray spectrometry (EDS) mapping analysis of heterostructure $VO_2$@GQD nanoarrays (scratched from FTO–$VO_2$@GQD sample) unambiguously confirms the existence of V, O and C elements and the homogeneous profile. All in all, it can be concluded that we have successfully achieved the integrated electrode based on the early-elaborated design.

**Lithium storage performance**

Our designed battery electrodes allow bicontinuous electron and lithium/sodium ion transfer channels through the GQD-GF network without the necessity of extra conductive additives, as schematically shown in Figure 3. During lithiation, electrolyte can enter the interval between nanoarrays on both outside and inner surface of GF, so that the Li/Na ion and electrons can react with the $VO_2$ nanoarrays directly. The GQDs coating provides two advantages: sensitization and protection. The first effect improves the ion diffusion and charge transport kinetics, thus beneficial to high-rate applications. For the protection function, the homogeneous GQDs covering can suppress the dissolution of $VO_2$ and agglomeration of the array, which is particularly important for long-term cycles. More discussion will be provided at the end.

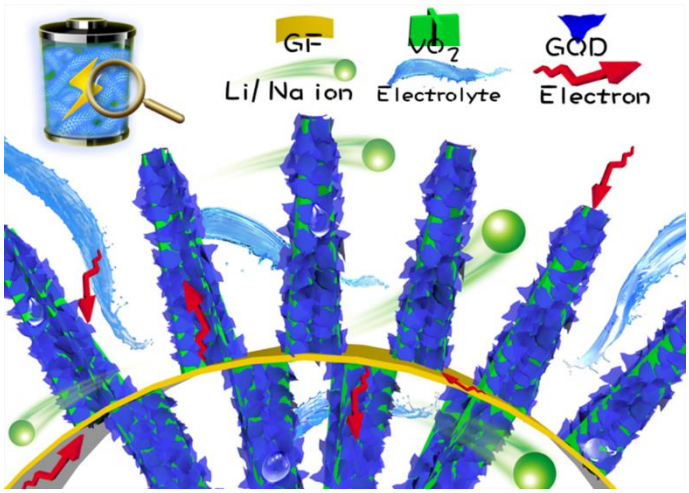


**Figure 3.** Schematic illustration of the GVG electrode with bicontinuous electron and Li/Na ion transfer channels.

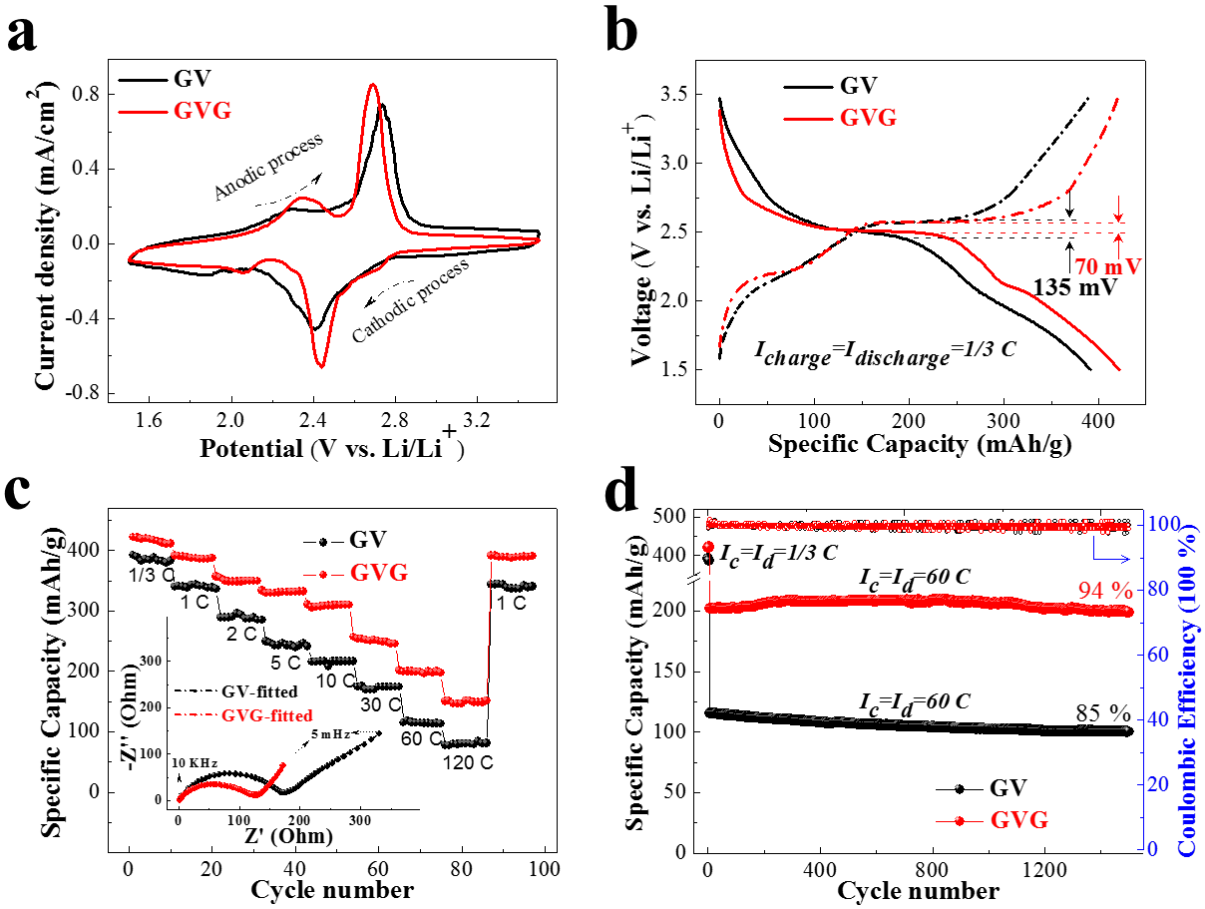


**Figure 4.** Electrochemical characterization for LIBs. (a,b) CV curves (scan rate 0.3 mV/s) and charge-discharge curves (1/3 C, 100 mA/g) after 5 cycles activation; (c) Rate performance of GV

and GVG electrodes. Inset is AC impedance plots at the full-charged state after the 1st cycle. The resistance is simulated using equivalent circuit of $R_S(Q(R_{ct}Z_W))$ (inset in Figure 5e), where $R_S$ is the ohmic resistance of solution and electrodes; $R_{ct}$ is the charge transfer resistance; $Q$ is the double layer capacitance and $Z_W$ is the Warburg impedance; (d) Cycling performance at 60 C for 1500 cycles (1/3 C at first 5 cycles for activation).

The CV tests of GV, and GVG electrodes for cathodic/anodic process (Figure 4a) were carried out at a sweep rate of 0.3 mV/s in the voltage range of 3.5 to 1.5 V versus $Li/Li^+$. As clearly shown in GV curves, a pair of distinctive redox peaks occurs around 2.40 and 2.73 V, accompany with several small redox peaks which indicate a multistep lithium ion intercalation/deintercalation. These redox peaks are consistent with the literature and could be related to the multiple valence states of the vanadium oxide.[35, 42] The overall lithium insertion/extraction process occurring in the $VO_2$ electrode could be described as (where x is the mole fraction of inserted Li ions):

$$VO_2 + xLi^+ + xe^- \leftrightarrow Li_xVO_2 \quad (3)$$

while GVG electrode delivers a positive cathodic peak (2.44 V) and a negative anodic peak (2.69 V) compared that of GV electrode. The difference in anodic and cathodic peaks is due to the increased surface electrochemical activity and the decreased polarization of the as-prepared GVG electrode. In order to evaluate the polarization more accurately, the overpotential is calculated from the difference between charge and discharge potential ($\Delta V_{Q/2}$) at the half reversible capacity (Q/2).[17] The overpotential of GVG electrode is only 70 mV, nearly half that of electrode without GQDs (135 mV), indicating higher electrical and ionic conductivity (Figure 4b and Figure S6: 45, 20, 35 S/cm for GF, GV and GVG, respectively). Electrochemical impedance spectroscopy (EIS) is employed to understand why the GVG electrode shows a better electrochemical activity (inset in Figure 4c). The charge transfer resistance ($R_{ct}$) of GV is ca. 190 Ω, while the corresponding $R_{ct}$ of GVG is only 120 Ω, suggesting its fast electronic mobility and improved electro-catalysis activity. Because of a higher electrochemical activity and better electron/ion transport kinetics, the GVG electrode has a higher specific capacity than that of the uncoated GF@VO2 electrode (421 mAh/g vs 391 mAh/g). A ca. 99% initial coulombic efficiency and 100% during the following cycles are obtained for all of the electrodes, implying an outstanding reversibility of the electrodes (Figure S7a,b in the Supporting Information).

To manifest the high-rate performance, the specific discharge capacities at different discharge/charge rates ranging from 1/3 C to 120 C have been tested (Figure 4c, Figure S7c,d). The GVG electrode deliveries discharge capacities of 421, 390, 349, 331, 309, 251, 198 and 151 mAh/g at the rate of 1/3 C, 1 C, 2 C, 5 C, 10 C, 30 C, 60 C and 120 C, respectively. These values are much higher than those of GV electrode without GQDs coating. After this high rate measurement, the GVG electrode is able to recover its original capacity (389 mAh/g) at 1 C, manifesting good rate reversibility. Such a high specific capacity and rate performance can be comparable to or higher than those of previous $VO_2$-based cathode materials (see detailed comparison in Table S1, the Supporting Information).

The integrated GVG electrodes have greatly enhanced long-cycle stability because of the improved electrical conductivity and likely shielding effect of GQDs in preventing dissolution of $VO_2$. The major bottleneck to $VO_2$ as the cathode material has been its unsatisfactory cycleability (Table S1). In previous reports, star-like $VO_2$ mesocrystals[21] and $VO_2$ hollow microsphere[43] gave capacity retentions of 76 % after 50 cycles and ca. 83 % after 50 cycles, respectively. Such fast drop in capacity may originate from the poor electric conductivity of the bare micro-sized materials. To overcome this drawback and improve the cyclability, nano-sized materials with different conductive additives have been prepared, such as $VO_2$/carbon nanobelts,[44] $VO_2$/graphene nanosheets,[45] and $VO_2$ nanotube/graphene.[35] However, the capacity retentions are still unsatisfactory even in short cycles (80% after 50 cycles, 60 % after 50 cycles, and 89 % after 20 cycles, respectively). Possible reasons include aggregation and gradual dissolution of the directly exposed active materials during the cycling process.[4, 42] In contrast, our GVG electrode delivers retention of 94 % of the original capacity after 1500 cycles at 60 C (18 A/g). Even the GV electrode without GQDs also has capacity retention of 85 % (see Figure 4d). Indeed the SEM examination of the electrode material after cycling shows that the array structure is better preserved compared to the uncoated GV electrode, with little aggregation or dissolution of the active material (shown in Figure S8).

**Sodium storage performance**

It is suggested that materials suitable for NIBs have tailored nanoarchitecture, more open framework and layered structure in order to accommodate larger volume changes compared to LIBs with smaller ion radius.[3, 22, 46] For these reasons, we thoroughly examined the sodium

storage performance based on the as-designed single-crystalline bilayered $VO_2$ nanostructure for the first time. Given the advantage of GQDs coating demonstrated above, herein we will make our characterization and discussion only based on the GVG electrode, and data are presented in Figure 5.

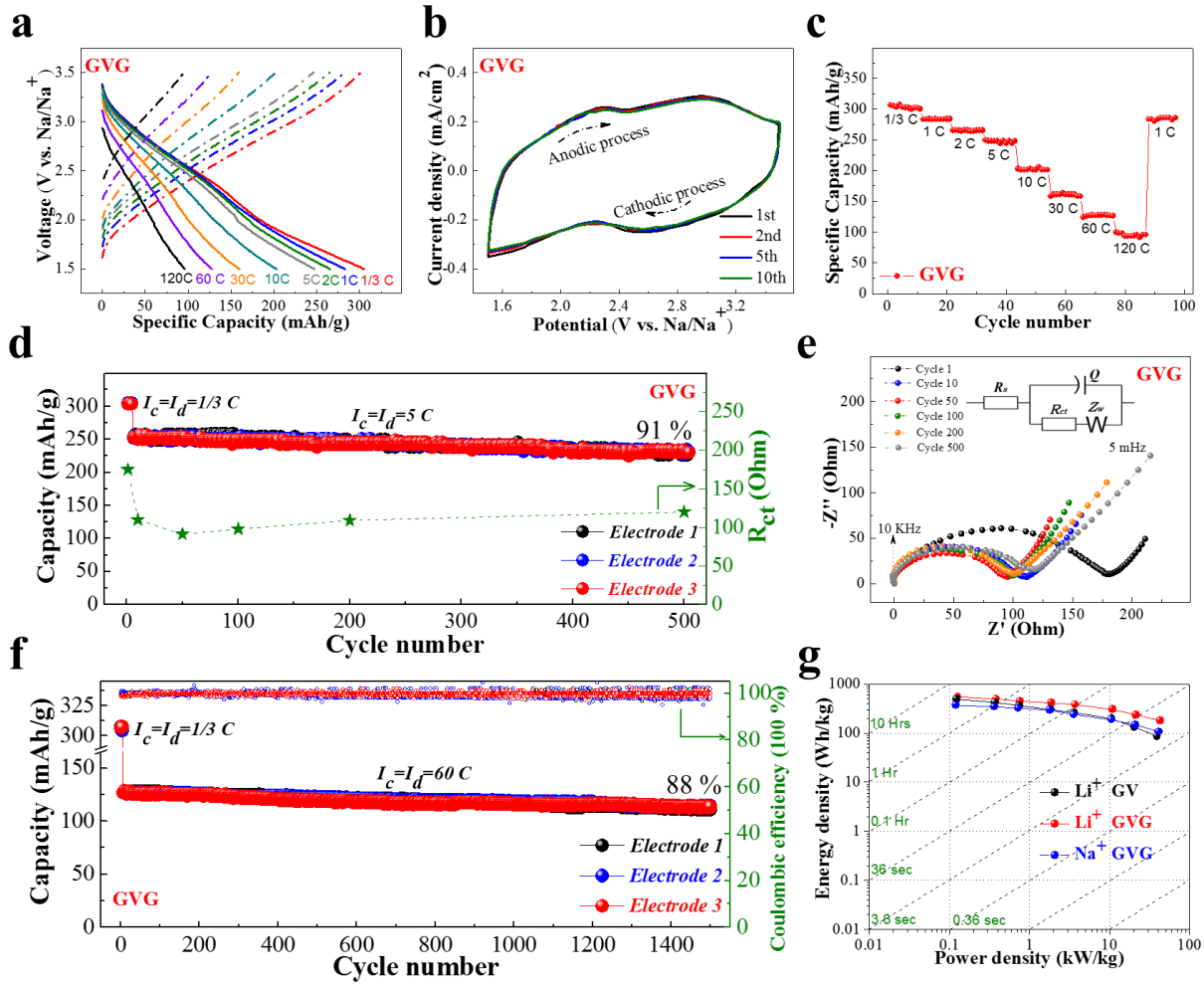


**Figure 5.** Electrochemical characterization for NIBs. (a) Charge-discharge curves at different C rates (1 C = 300 mA/g); (b) CV curves at a scan rate of 0.3 mV/s; (c) Rate tolerance performance of the GVG electrode; (d) Cycling performance of three different GVG electrodes at 5 C for 500 cycles. The $R_{ct}$ as a function of cycle number is also shown. (e) AC impedance plots at full-charged state after different cycles. The resistance is simulated using the same equivalent circuit $R_S(Q(R_{ct}Z_W)$ (inset in Figure 5e) as used in LIBs; (f) Cycling performance of three different electrodes at 60 C for 1500 cycles (1/3 C at first 5 cycles for activation); (g) Ragone plot based on the total mass of the whole electrode, the sloping lines indicate the relative time to get the charge in or out of the electrodes.

The GVG electrode delivers a very high discharge capacity of 306 mAh/g at 1/3 C (100 mA/g) in the voltage range of 3.5 to 1.5 V versus $Na/Na^+$. It is noted that the discharge profile in Figure 5a shows no obvious plateau as a whole. But the slopes still can be divided into two diagonal stages (Stage 1: 2.7–2.4 V; Stage 2: 1.9–1.6 V) for different sodium intercalation processes:

$$VO_2 + xNa^+ + xe^- \leftrightarrow Na_xVO_2 \quad (4)$$

where x is the mole fraction of inserted Na ions. The CV curves in Figure 5b exhibit only two small broaden peaks during cathodic processes (Peak 1: 2.7–2.4 V, and Peak 2: 1.9–1.6 V), in accordance to the charge/discharge profiles. Reversible sodium deintercalation process is obtained by charging the electrode to 3.5 V (ca. 99 % initial coulombic efficiency and 100% in the following cycles), demonstrating a stable GVG electrode during the $Na^+$ insertion and extraction processes (Figure 5b). On the other hand, the quasi-linear discharge curves and broad redox peaks in CV curves also indicate a pseudocapacitive (surface Faradic reaction) behavior in our GVG electrode.[47-50] This is reasonable to think that the pseudocapacitive process in metal oxides can play an important role especially when the metal oxide particle sizes scale down to nanosize and/or at high porosities.[50]

The uniquely designed electrode allows us to push the rate tolerance capability in Na ion storage. Most materials used for LIB electrodes may not work equally well for NIBs because of a sluggish electrochemical kinetics with Na ions. Previous research on NIBs all demonstrated capacities at relatively low rates of 0.1–5 C (see complete list in Table S2).[3, 13, 22, 25, 51-53] In this work, the judiciously designed GVG electrode structure allows us to charge/discharge at really high current densities ranging from 1/3 to 120 C. When cycled at high rate: 1 C, 2 C, 5 C, 10 C, 30 C, 60 C and 120 C, it can achieve a remarkably stable and high capacity of 284, 265, 247, 201, 160, 127 and 93 mAh/g, respectively, and then recovers to 281 mAh/g at 1 C (Figure 5c). This is in sharp contrast to those reported $VO_x$ electrode: bilayered $V_2O_5$ nanoparticles,[3] bilayered $V_2O_5$ nanobelts,[22] $VO_x$/Ni nanotubes[54] and amorphous $V_2O_5$ film[55] (listed in Table S2).

The sodium-ion devices based on the GVG electrode retained 91 % of the initial capacity after 500 cycles at a charge/discharge rate of 5 C (Figure 5d). We tested three batches of GVG electrodes and the result is fairly reproducible. To gain further insight into the electrode changes upon sodium ion insertion/extraction cycles, the EIS is monitored during 1$^{st}$ to 500$^{th}$ cycles. The

fitted sodium charge transfer resistances ($R_{ct}$) corresponding to the Nyquist plots are shown in Figure 5d. It should be noted that the $R_{ct}$ values decrease steeply in the first 50 cycles and then increase slightly in the following cycles. We propose that electrolyte gradually penetrated on the surface of nanobelts array and diffused into the predominantly exposed (001) facets after the first few cycles which should facilitate the electrochemical reaction and lead to the decrease of $R_{ct}$. It is well-known that the slower increase of resistance during cycles means lower polarization. Hence, the subsequent mild $R_{ct}$ increase perfectly illustrates the good cycling behavior of the electrode.

To demonstrate the high-power application potential of the GVG electrode, we tested the long-term ultrafast charge/discharge cycling. Figure 5f shows that, even after 1500 cycles at the rate of 60 C, the discharge capacity can be stabilized at 111 mAh/g, delivering over 88 % capacity retention. This performance is superior to previous NIB cathodes reported to date (see comparison in Table S2). The ultra-long cycling tolerance and high rate capability should be related to both the structure stability and pseudocapacitive behavior of the GVG electrode.[46] Furthermore, at the ultrahigh rate of 120 C, the power density based on mass of the whole GVG electrode is as high as 42 kW/kg with an energy density of more than 100 Wh/kg (Figure 5g). Assuming that the cathode takes up ca. 40% of the total device weight, the power density is still as high as 16 kW/kg.[15, 46]

Discussion on advantageous feature of this integrated electrode is provided as follows. The outstanding electrochemical performance of $VO_2$–based cathode material in NIBs is related to the unique long-range order, single-crystalline and thin nanobelt morphology of the $VO_2$. The large interlayer spacing and exposed facets provide open channels for facile sodiation/desodiation. The layer of surface functionized GQDs makes the $VO_2$ surface lipophilic, so that it facilitates the penetration of electrolyte and ion transfer, and therefore enhances the reaction kinetics. In addition to this “sensitization” effect, the homogeneous GQDs coating can also prevent the dissolution of $VO_2$ by decreasing the exposed physical surfaces of $VO_2$. Furthermore, MD simulations using the reactive force field (ReaxFF) potential[4] suggests an enhanced structure stability supported by the formation of covalent bonds between the GQD and $VO_2$ slab (Figure S9 and details of the simulation parameters). This may further corroborate the enhanced nanostructure stability during long-term electrochemical reactions. Finally, the nanocavities between the stacked GQDs would offer favorable transport routes for Na ions,[34, 56]

and simultaneously provide a nontrivial contribution to the capacity due to physical adsorption of $Na^+$ between the GQDs (see schematics in Figure S10). We are optimistic that this ultrafast charging/discharging capability can significantly boost the development of high-rate and long lifespan LIBs and NIBs.

In conclusion, we have demonstrated high capacity, high-rate and durable lithium and sodium ion storage performance using single-crystalline long-range-ordered bilayered $VO_2$ nanoarray electrodes. The $VO_2$ nanoarrays are bottom-up grown on double-face graphene foam, forming self-supported, binder-free electrode for both devices. Interestingly, coating the $VO_2$ array by a thin (~2 nm) additional GQDs layer brings further advantages in enhancing the electrochemical performance both in LIBs and NIBs. The GQDs layer may work as a surface sensitizer and protector. In lithiation, our GVG electrode delivers a capacity more than 420 mAh/g and a capacity retention of 94 % after 1500 cycles at 18 A/g. During sodiation, it can also exhibit a high capacity of 306 mAh/g and superior rate tolerance, and good capacity retention (88 % after 1500 cycles at 18 A/g), with a power density of 42 kW/kg at an energy density more than 100 Wh/kg. Our results might be a milestone in the development of rechargeable NIBs with a comparable performance to the present LIBs, thus pushing NIB as a cost-effective alternative for next-generation postlithium (e.g., Na and Mg) batteries.

**Experimental**

**Growth of Bilayered $VO_2$ Arrays by Solvothermal Method.** Vanadium oxide was synthesized according to our previously reported method with modification.[16] Firstly, 1.2 g $V_2O_5$ powder (Sigma-Aldrich) and 1.8 g $H_2C_2O_4$ powder (Sigma-Aldrich) were dissolved with 40 mL of distilled water at 75 ℃ until a dark blue solution was formed. 5 mL of the above solution was transferred into a 30 mL Teflon-lined stainless steel autoclave. Then 1 mL of 30 % $H_2O_2$ and 20 mL ethanol was added and kept continuously stirring for about 20 min. And then, one piece of 3D graphene foam (GF, 2×5 cm, ca. 0.6 mg $cm^{-2}$, prepared by CVD method according to our previously results[16, 57]) was immersed into the reaction solution. The autoclave liners was kept at 180 ℃ for 3 h, and then the sample was collected and rinsed with ethanol and distilled water in turn for three times. Finally, the samples were dried at 120 ℃ in vacuum to obtain bilayered $VO_2$ array (0.6 mg $cm^{-2}$).

**Preparation of $VO_2$@GQD Arrays.** 150 mg graphene oxide (GO, by a modified Hummers method) was dispersed in 20 mL DMF (under ultrasonication for 30 minutes). The solution was transferred into a 30

mL Teflon-lined stainless steel autoclave and heated at 200 ℃ for 8 h. After being cooled down naturally, the mixture was filtered using a 0.22 μm microporous membrane and the obtained brown solution was functional GQDs dispersion in DMF. The solvent of suspension was removed with the aid of a rotary evaporator at 80 ℃ under reduced pressure. $VO_2$@GQD arrays can be obtained in the help of a facile electrophoresis process by dispersing the functional GQD in DI water. The above GF supported $VO_2$ arrays were used as the substrate (working electrode) for the growth of $VO_2$@GQD arrays, and Pt plate was used as counter electrode. And then a positive potential of 6 V for different time in the condition of ice-bath was applied to deposit functional GQDs onto the surface of $VO_2$ arrays. Finally, the samples were annealed at 400 ℃ in Ar for 2 h to obtain good structure stability. As a comparison, $VO_2$@GQD arrays were also fabricated on transparent conductive fluorine-tin-oxide (FTO) substrates using the same methods as described above. The weight increase (measured by an analytical balance, RADWAG, MYA 21, d=1μg) after GQDs deposition was ca. 30 μg (ca. 5 % weight of $VO_2$ arrays). The typical weight fraction of $VO_2$ in the whole electrode is ~49%. The surface area of the whole GVG electrode and pure GF were determined by $N_2$ adsorption/desorption isotherms to be ~147 and ~28 $m^2/g$, respectively.

**Characterization of GF Supported $VO_2$@GQD Arrays.** The crystal structures of the samples were identified using X-ray diffraction (XRD, RigakuD/Max-2550 with Cu Kα radiation). Raman spectra were obtained with a WITec-CRM200 Raman system (WITec, Germany) with a laser wavelength of 532 nm (2.33 eV). The Si peak at 520 $cm^{-1}$ was used as a reference to calibrate the wavenumber. The morphologies of the samples were characterized by field emission scanning electron microscopy. The structures of the samples were investigated by high-resolution transmission electron microscopy (HRTEM, JEOL JEM-2010F at 200 kV).

**Battery Fabrication and Electrochemical Measurements.** Standard CR2032-type coin cells were assembled in an argon-filled glove box (Mbraun, Unilab, Germany) with the as-fabricated GF supported $VO_2$@GQD nanoarrays as the working electrode (with diameter of 12 mm, without any binder or additives). For lithium ion battery fabrication, the metallic lithium foil as the counter-electrode, 1 M LiPF6 in ethylene carbonate (EC)–dimethyl carbonate (DME) (1:1 in volume) as the electrolyte, and a polypropylene (PP) film (Cellgard 2400) as the separator; For sodium ion battery fabrication, the metallic sodium foil as the counter-electrode, 1 M NaPF6 in ethylene carbonate (EC)–diethyl carbonate (DEC)–fluoroethylene carbonate (FEC) (1:1:0.05 in volume) as the electrolyte, and glass fiber as the separator. The CV measurements were carried out using a Parstat-2273 electrochemical potentiostat at a scanning rate of 0.3 mV/s. For electrochemical impedance spectroscopy (EIS), the amplitude of the sine perturbation signal was 5 mV, and the frequency was scanned from the highest (10 kHz) to the lowest (5 mHz). Galvanostatic charge discharge cycles were tested by Neware battery tester at different current densities at room temperature.

## ASSOCIATED CONTENT

*Supporting Information Available:* More SEM images of GQDs coverage (**Figure S1**), large-scale SEM images of the electrodes at different fabrication stages and corresponding photographs (**Figure S2**), XRD, Raman and EDX spectra of the electrodes (**Figure S3**), enlarged TEM image of the GQDs on $VO_2$ nanorod surface (**Figure S4**), atomic model of $VO_2$ (**Figure S5**), electrical conductivities of three electrodes (**Figure S6**), CV and charge/discharge curves (**Figure S7**), electrode morphology after $Li^+$ insertion/extraction for 1500 cycles (**Figure S8**), MD simulation (**Figure S9**), electrochemical property of GQDs directly on GF (**Figure S10**), surveys of $VO_2$-based electrodes for Li-ion batteries and Na-ion batteries (**Table S1 and S2**). This material is available free of charge *via* the Internet at http://pubs.acs.org.

## AUTHOR INFORMATION

**Corresponding Authors**.

Email: zexiang@ntu.edu.sg (Z. X. S)

Email: fanhj@ntu.edu.sg (H.J. F);

### Author contributions

D.L. Chao and C.R. Zhu contributed equally to this work.

### Notes

The authors declare no competing financial interest.

## ACKNOWLEDGEMENTS

This work is supported by SERC Public Sector Research Funding (Grant number 1121202012), Agency for Science, Technology, and Research (A*STAR), and MOE AcRF Tier 1 (RG104/14). H. Zhang thanks the support from MOE AcRF Tier 2 (ARC 26/13, No. MOE2013-T2-1-034) and AcRF Tier 1 (RG61/12, RGT18/13, RG5/13), and Start-up Grant (M4080865.070) in Singapore. This Research is also conducted by NTU-HUJ-BGU Nanomaterials for Energy and Water Management Programme under the Campus for Research Excellence and Technological Enterprise (CREATE), which is supported by the National Research Foundation, Prime Minister's Office, Singapore. We thank Yu Ting for help with battery assembly.

## References and notes


1. Gershinsky, G.; Bar, E.; Monconduit, L.; Zitoun, D. *Energy Environ. Sci.* **2014,** 7, 2012-2016.
2. Xie, J. L.; Guo, C. X.; Li, C. M. *Energy Environ. Sci.* **2014,** 7, 2559-2579.
3. Tepavcevic, S.; Xiong, H.; Stamenkovic, V. R.; Zuo, X. B.; Balasubramanian, M.; Prakapenka, V. B.; Johnson, C. S.; Rajh, T. *ACS nano* **2012,** 6, 530-538.
4. Yan, M.; Wang, F.; Han, C.; Ma, X.; Xu, X.; An, Q.; Xu, L.; Niu, C.; Zhao, Y.; Tian, X.; Hu, P.; Wu, H.; Mai, L. *J. Am. Chem. Soc.* **2013,** 135, 18176-18182.
5. Reddy, M. V.; Subba Rao, G. V.; Chowdari, B. V. *Chem. Rev.* **2013,** 113, 5364-5457.
6. Choi, N. S.; Chen, Z.; Freunberger, S. A.; Ji, X.; Sun, Y. K.; Amine, K.; Yushin, G.; Nazar, L. F.; Cho, J.; Bruce, P. G. *Angew. Chem. Int. Ed.* **2012,** 51, 9994-10024.
7. Goodenough, J. B.; Park, K.-S. *J. Am. Chem. Soc.* **2013,** 135, 1167-1176.
8. Ong, S. P.; Chevrier, V. L.; Hautier, G.; Jain, A.; Moore, C.; Kim, S.; Ma, X. H.; Ceder, G. *Energy Environ. Sci.* **2011,** 4, 3680-3688.
9. Berthelot, R.; Carlier, D.; Delmas, C. *Nat. Mater.* **2011,** 10, 74-80.
10. Yabuuchi, N.; Kajiyama, M.; Iwatate, J.; Nishikawa, H.; Hitomi, S.; Okuyama, R.; Usui, R.; Yamada, Y.; Komaba, S. *Nat. Mater.* **2012,** 11, 512-517.
11. Wang, L.; Lu, Y.; Liu, J.; Xu, M.; Cheng, J.; Zhang, D.; Goodenough, J. B. *Angew. Chem. Int. Ed.* **2013,** 52, 1964-1967.
12. Li, S.; Dong, Y.; Xu, L.; Xu, X.; He, L.; Mai, L. *Adv. Mater.* **2014,** 26, 3545-3553.
13. Li, C.; Yin, C.; Gu, L.; Dinnebier, R. E.; Mu, X.; van Aken, P. A.; Maier, J. *J. Am. Chem. Soc.* **2013,** 135, 11425-11428.
14. Liu, J.; xia, H.; Xue, D.; Lu, L. *J. Am. Chem. Soc.* **2009,** 131, 12086-12087.
15. Yang, S.; Gong, Y.; Liu, Z.; Zhan, L.; Hashim, D. P.; Ma, L.; Vajtai, R.; Ajayan, P. M. *Nano Lett.* **2013,** 13, 1596-1601.
16. Chao, D.; Xia, X.; Liu, J.; Fan, Z.; Ng, C. F.; Lin, J.; Zhang, H.; Shen, Z. X.; Fan, H. J. *Adv. Mater.* **2014,** 26, 5794-5800.
17. Niu, C.; Meng, J.; Han, C.; Zhao, K.; Yan, M.; Mai, L. *Nano Lett.* **2014,** 14, 2873-2878.
18. C. Tsang; Manthiram, A. *J. Electrochem. Soc.* **1997,** 144, 520-524.
19. Zhang, L.; Zhao, K.; Xu, W.; Meng, J.; He, L.; An, Q.; Xu, X.; Luo, Y.; Zhao, T.; Mai, L. *RSC Adv.* **2014,** 4, 33332-33337.
20. Mai, L.; Wei, Q.; An, Q.; Tian, X.; Zhao, Y.; Xu, X.; Xu, L.; Chang, L.; Zhang, Q. *Adv. Mater.* **2013,** 25, 2969-2973.
21. Uchaker, E.; Gu, M.; Zhou, N.; Li, Y.; Wang, C.; Cao, G. *Small* **2013,** 9, 3880-3886.
22. Su, D.; Wang, G. *ACS nano* **2013,** 7, 11218-11226.
23. Wenzel, S.; Hara, T.; Janek, J.; Adelhelm, P. *Energy Environ. Sci.* **2011,** 4, 3342-3345.
24. Alcántara, R.; Jiménez-Mateos, J. M.; Lavela, P.; Tirado, J. L. *Electrochem. Commun.* **2001,** 3, 639-642.
25. Sun, Y.; Zhao, L.; Pan, H.; Lu, X.; Gu, L.; Hu, Y. S.; Li, H.; Armand, M.; Ikuhara, Y.; Chen, L.; Huang, X. *Nat. Commun.* **2013,** 4, 1870-1879.
26. Yuan, S.; Huang, X. L.; Ma, D. L.; Wang, H. G.; Meng, F. Z.; Zhang, X. B. *Adv. Mater.* **2014,** 26, 2273-2279.
27. Zhang, Z. P.; Zhang, J.; Chen, N.; Qu, L. T. *Energy Environ. Sci.* **2012,** 5, 8869-8890.
28. Son, D. I.; Kwon, B. W.; Park, D. H.; Seo, W. S.; Yi, Y.; Angadi, B.; Lee, C. L.; Choi, W. K. *Nat. Nanotechnol.* **2012,** 7, 465-471.
29. Lin, J.; Zhang, C.; Yan, Z.; Zhu, Y.; Peng, Z.; Hauge, R. H.; Natelson, D.; Tour, J. M. *Nano Lett.* **2013,** 13, 72-78.
30. Gao, P.; Ding, K.; Wang, Y.; Ruan, K.; Diao, S.; Zhang, Q.; Sun, B.; Jie, J. *J. Phys. Chem. C* **2014,** 118, 5164-5171.
31. Tian, J.; Zhao, H.; Quan, X.; Zhang, Y.; Yu, H.; Chen, S. *Sens. Actuators B: Chem.* **2014,** 196, 532-538.
32. Zhou, X.; Tian, Z.; Li, J.; Ruan, H.; Ma, Y.; Yang, Z.; Qu, Y. *Nanoscale* **2014,** 6, 2603-2607.
33. Ananthanarayanan, A.; Wang, X. W.; Routh, P.; Sana, B.; Lim, S.; Kim, D. H.; Lim, K. H.; Li, J.; Chen, P. *Adv. Funct. Mater.* **2014,** 24, 3021-3026.
34. Slater, M. D.; Kim, D.; Lee, E.; Johnson, C. S. *Adv. Funct. Mater.* **2013,** 23, 947-958.
35. Nethravathi, C.; Viswanath, B.; Michael, J.; Rajamath, M. *Carbon* **2012,** 50, 4839-4846.

36. Yuwono, V. M.; Burrows, N. D.; Soltis, J. A.; Penn, R. L. *J. Am. Chem. Soc.* **2010,** 132, 2163-2165.
37. Wang, H. W.; Yi, H.; Chen, X.; Wang, X. F. *J. Mater. Chem. A* **2014,** 2, 1165-1173.
38. Son, Y.-W.; Cohen, M. L.; Louie, S. G. *Phys. Rev. Lett.* **2006,** 97, 216803.
39. Nakada, K.; Fujita, M.; Dresselhaus, G.; Dresselhaus, M. S. *Phys. Rev. B* **1996,** 54, 17954-17961.
40. Liu, W.-W.; Feng, Y.-Q.; Yan, X.-B.; Chen, J.-T.; Xue, Q.-J. *Adv. Funct. Mater.* **2013,** 23, 4111-4122.
41. Liu, J.; Li, Q.; Wang, T.; Yu, D.; Li, Y. *Angew. Chem. Int. Ed.* **2004,** 43, 5048-5052.
42. Zhao, Q.; Jiao, L.; Peng, W.; Gao, H.; Yang, J.; Wang, Q.; Du, H.; Li, L.; Qi, Z.; Si, Y.; Wang, Y.; Yuan, H. *J. Power Sources* **2012,** 199, 350-354.
43. Liu, H. M.; Wang, Y. G.; Wang, K. X.; Hosono, E.; Zhou, H. S. *J. Mater. Chem.* **2009,** 19, 2835-2840.
44. Rui, X.; Sim, D.; Xu, C.; Liu, W.; Tan, H.; Wong, K.; Hng, H. H.; Lim, T. M.; Yan, Q. *RSC Advances* **2012,** 2, 1174-1180.
45. Nethravathi, C.; Rajamathi, C. R.; Rajamathi, M.; Gautam, U. K.; Wang, X.; Golberg, D.; Bando, Y. *ACS Appl. Mater. Interfaces* **2013,** 5, 2708-2714.
46. Chen, Z.; Augustyn, V.; Jia, X.; Xiao, Q.; Dunn, B.; Lu, Y. *ACS nano* **2012,** 6, 4319-4327.
47. Sathiya, M.; Prakash, A.; Ramesha, K.; Tarascon, J. M.; Shukla, A. *J. Am. Chem. Soc.* **2011,** 133, 16291-16299.
48. Yan, Z.; Liu, L.; Tan, J.; Zhou, Q.; Huang, Z.; Xia, D.; Shu, H.; Yang, X.; Wang, X. *J. Power Sources* **2014,** 269, 37-45.
49. Armstrong, A. R.; Arrouvel, C.; Gentili, V.; Parker, S. C.; Islam, M. S.; Bruce, P. G. *Chem. Mater.* **2010,** 22, 6426-6432.
50. Simon, P.; Gogotsi, Y.; Dunn, B. *Science* **2014,** 343, 1210-1211.
51. Wen, Y.; He, K.; Zhu, Y.; Han, F.; Xu, Y.; Matsuda, I.; Ishii, Y.; Cumings, J.; Wang, C. *Nat. Commun.* **2014,** 5, 4033-4042.
52. Yu, D. Y.; Prikhodchenko, P. V.; Mason, C. W.; Batabyal, S. K.; Gun, J.; Sladkevich, S.; Medvedev, A. G.; Lev, O. *Nat. Commun.* **2013,** 4, 2922-2928.
53. Abouimrane, A.; Dambournet, D.; Chapman, K. W.; Chupas, P. J.; Weng, W.; Amine, K. *J. Am. Chem. Soc.* **2012,** 134, 4505-4508.
54. Kim, H.; Kim, R. H.; Lee, S. S.; Kim, Y.; Kim, D. Y.; Park, K. *ACS Appl. Mater. Interfaces* **2014,** 6, 11692-11697.
55. Uchaker, E.; Zheng, Y.-Z.; Li, S.; Candelaria, S. L.; Hu, S.; Cao, G. *J. Mater. Chem. A* **2014,** 2, 18208-18214.
56. Yan, Y.; Yin, Y. X.; Guo, Y. G.; Wan, L. J. *Adv. Energy Mater.* **2014,** 4, 1301584.
57. Xia, X. H.; Chao, D. L.; Fan, Z. X.; Guan, C.; Cao, X. H.; Zhang, H.; Fan, H. J. *Nano Lett.* **2014,** 14, 1651-1658.

TOC